Hua, K.; Zhang, Y.; Gan, W.; Kou, H.; Beausir, B.; Li, J.; Esling, C.:
Hot deformation behavior originated from dislocation activity and β to α phase transformation in a metastable β titanium alloy.
In: International Journal of Plasticity. Vol. 119 (2019) 200 - 214.

First published online by Elsevier: 28.03.2019

https://dx.doi.org/10.1016/j.ijplas.2019.03.011

Hot deformation behavior originated from dislocation activity and β to α phase transformation in a metastable β titanium alloy

Ke Hua[a,b,c], Yudong Zhang[b,c]*, Weimin Gan[d], Hongchao Kou[a]*, Benoit Beausir[b,c], Jinshan Li[a]*, and Claude Esling[b,c]

[a] State Key Laboratory of Solidification Processing, Northwestern Polytechnical University, 710072 Xi'an, PR China

[b] Université de Lorraine, CNRS, Arts et Métiers ParisTech, LEM3, F-57000 Metz, France

[c] Laboratory of Excellence on Design of Alloy Metals for low-mAss Structures (DAMAS), Université de Lorraine, 57073 Metz, France

[d] German Engineering Materials Science Center at MLZ, Helmholtz-Center Geesthacht, D-85748 Garching, Germany

* Corresponding authors:

E-mail: yudong.zhang@univ-lorraine.fr (Yudong Zhang);

hchkou@nwpu.edu.cn (Hongchao Kou)

ljsh@nwpu.edu.cn (Jinshan Li)

Abstracts

Profound and comprehensive knowledge on hot deformation of metastable β titanium alloy is essential to process optimization and microstructure control. In this work, the hot compression behavior of a β quenched metastable β titanium alloy is thoroughly studied by examining microstructural evolution to resolve the related deformation mechanisms. It is demonstrated that the deformation of the alloy presents three characteristic stress-strain stages: a linear stage (Stage I), a discontinuous yielding (Stage II) and a steady-state (Stage III). Before and during Stage I, the β to α phase transformation happened intensively along the β grain boundaries with more than 90% of the boundaries occupied by grain boundaries α (α_{GB}). The linear behavior deviates from the Young's modulus when the linear deformation proceeds to the late stage, indicating the onset of plastic deformation. This behavior results from dislocation slip near β grain boundary regions. The discontinuous yielding of Stage II is originated from the fragmentation of the α_{GB} and the intensive formation of mobile dislocations near the β grain boundary areas. The steady-state of Stage III arises from two orientation dependent deformation modes of the β grains. For those in favorable activation orientation for their $\{110\}_\beta\langle 1\bar{1}1\rangle_\beta$ systems with respect to the external compressive load (type I), the deformation is realized by the dislocation slip and by the formation of slip bands; whereas for those with their $\{1\bar{1}\bar{2}\}_\beta\langle\bar{1}1\bar{1}\rangle_\beta$ systems - the major lattice deformation for structure change from β to α - in favorable activation orientations (type II), the deformation is achieved by intensive phase transformation by forming intragranular α precipitates. The present results provide new information

on hot deformation mechanisms of metastable β titanium alloys, especially the phase transformation associated lattice deformation as an important plastic deformation mode.

Key words:

Phase transformation (A); Electron microscopy (EBSD/TEM) (C); Microstructures (A); Dislocations (A); Titanium alloy.

1. Introduction

Hot working is an important processing procedure for metal forming and mechanical property optimization, and thus widely used for the manufacturing of metallic materials, such as steels (Eyckens et al., 2015; Fujita et al., 2018; Khan et al., 2016; Kestens and Pirgazi, 2016; Pham et al., 2015; Tasan et al., 2014), Titanium alloys (Khan et al., 2004, 2007; Liu et al., 2015; Mandal et al., 2017; Meredith et al., 2012), Aluminum alloys (Sidor et al., 2015; Sun et al., 2018), and NiTi shape memory alloys (Wang et al., 2017; Xiao et al., 2018). During the process, two opposite effects - hardening from crystal defect multiplication and crystal reorientation, and softening from defect rearrangement or annihilation via recovery and recrystallization - interweave, resulting in characteristic stress-strain behavior and microstructure evolution. Thus the mechanical responses of the alloys during thermomechanical processes have been a topic of intensive experimental and theoretical investigations for process optimization and microstructure and mechanical property improvement. Among the metallic materials, the metastable β titanium alloys are of particular interest for structural applications in aerospace and biomedicine (Bonisch et al., 2017; Boyer, 2010; Lütjering and Williams, 2007), and hot working by rolling or forging is routinely used for their manufacturing. Thus, numerous studies have been devoted to conceiving novel thermo-mechanical processes, and to revealing the hot deformation behavior and the microstructure evolution.

So far, the investigations on hot deformation of metastable titanium alloys have been focused on deformation either in the single β phase region (>T_β (β transus

temperature)) or in the α+β two phase region (<T_β). For the former, only the β phase is concerned. The investigations have been mainly on the effect of deformation parameters, such as deformation strain rate, on microstructure evolution by recovery and/or recrystallization and texture change of the β phase (Furuhara et al., 2007; Rollett et al., 2017; Kanjarla et al., 2010; Matsumoto et al., 2014). For the hot deformation conducted in the α+β two phase region, the initial microstructure consists of the two phases, β and α. Since the deformation temperature (usually from 873K to 1023K) is close to the processing temperature (usually from 973K to 1123K), the topic has received much attention. Many investigations have been conducted on the deformation behavior of the alloys and the effect of deformation variables on microstructure evolution and on the underlying mechanisms. It has been revealed that the hot deformation (compression) behavior of metastable β alloys in this region is always characterized first by a linear stress-strain state, then by a drastic stress drop (termed discontinuous yielding) and finally by a steady-state (Mandal et al., 2017). The discontinuous yielding is a typical behavior not only of metastable β titanium alloys (Jing et al., 2017; Jonas et al., 2017; Koike et al., 2000; Philippart and Rack, 1998; Srinivasan, 1992) but also of zirconium alloys (Jonas et al., 1979). It has been proved to be a result of the stress induced reverse phase transformation (α→β) (Jing et al., 2017; Jonas et al., 2017; Koike et al., 2000), or to be related to the generation of mobile dislocations at the grain boundary regions (Philippart and Rack, 1998; Srinivasan, 1992), depending on the alloy composition. The steady-state is found to be a result of a counterbalance between work hardening and work softening.

Dislocation slip has been considered as the main deformation mechanism and the dynamic recovery is the dominant mechanism for restoration of the β phase (Jones et al., 2008, 2009; Johnston and Gilman, 1959; Pham et al., 2015; Rollett et al., 2015). In addition to the dislocation activity, the effects of the secondary phase (α phase), especially its distribution, size and morphology, on deformation behavior have also been examined (Jones et al., 2008, 2009; Ozturk and Rollet, 2018; Poletti et al., 2016; Warchomicka et al., 2006; Weiss and Semiatin, 1998).

Despite the large amount of experimental investigations and theoretical simulations, the hot deformation of metastable β titanium alloys with an initial single β phase in the α+β two phase region has seldom been addressed. The deformation process should be more complicated as the β to α phase transformation happens naturally in this temperature region. Although the β to α phase transformation and α variant selection criteria during hot deformation have been intensively studied both experimentally (Bohemen et al., 2008; Hua et al., 2018) and theoretically (Shi and Wang, 2013), the influence of the transformation, especially the transformation associated lattice deformation, on the mechanical response of the alloy has not yet been reported.

Based on such an observation, we conducted the present work with an aim to correlate the microstructure evolution with the hot compression stress-strain behavior of a β quenched metastable β titanium alloy (Ti-7333) to resolve the underlying mechanisms of the hot deformation behavior of the alloy. Special efforts have been made to the contribution of the β to α phase transformation at different deformation

stages. Especially, for the steady state of deformation, the results of our previous work on variant selection of intragranular α precipitates under the same hot compression condition and on the associated lattice deformation feature (Hua et al., 2018) provided a solid basis for the present work to specify the role of the phase transformation as another kind of deformation mechanism for crystal plasticity. To obtain accurate and statistical experimental evidences, in-situ and ex-situ multiscale characterization techniques have been utilized and the examinations have been made on large sample volume or areas. This study is expected to provide more information to enrich the fundamental knowledge on hot deformation of Ti alloys and to offer experimental data for theoretical simulation utilizing various mechanical models.

2. Experimental procedures

The material used in the present work is hot forged Ti-7Mo-3Nb-3Cr-3Al (in wt. %). Cylindrical specimens with dimensions of Φ10 x 15 mm were cut out of the forged bar and solution-treated at 1173 K (T_β ~ 1123 K. T_β is the β transus temperature) for 30 minutes and quenched in water to obtain a homogeneous single β phase as the initial microstructure.

The as-solution treated specimens were then subjected to unidirectional isothermal compression using a Gleeble-3500 thermo-mechanical simulator system under vacuum (to prevent oxidation of the specimen and also the parts of the deformation frame of the Gleeble system exposed to the heat). The specimens were first heated to 973 K (the compression temperature) at a rate of 25 K/s and held for 5 s

to homogenize the temperature, and then they were compressed at a strain rate of 10^{-3} s^{-1} (that corresponds to a constant cross-head speed (mm/s) in the Gleeble simulator system) to the true strains of 0.015, 0.03 and 0.35, respectively. After being strained, the specimens were immediately quenched in water to preserve the deformed microstructure. In order to reduce friction and maintain a uniform deformation, two pieces of thin tantalum sheets were placed between the specimen and the compression die. The microstructural and crystallographic features of the deformed specimen were examined by post mortem characterization techniques from the macroscopic scale to the microscopic scale to ensure a statistical relevance of the results. For the phase constituents and the morphological features, the deformed specimens were examined using a Jeol JMF6500-F SEM. For the crystallographic features, the deformed regions were analyzed using a Jeol JMF6500-F SEM equipped with an EBSD camera and the Aztec online acquisition software package (Oxford Instruments). The orientations of the fine microstructural constituents (α precipitates) were measured manually and the coarse constituents (β grains) were measured automatically by EBSD. The data were processed using Channel 5 (Oxford Instruments) and ATEX software (Beausir and Fundenberger, 2017). The examined total area (1.7×3 mm^2) covers the whole homogeneous deformation region in the cross section of the deformed specimen. To achieve the surface quality of the specimens for SEM and SEM-EBSD measurements, the specimens were first mechanically polished and then electrolytically polished with a solution of 10% perchloric acid in methanol at 35 V for 5 s at temperatures lower than 5°C. For the fine microstructure features of the deformed specimen, the

examinations were performed using a Philips CM200 TEM equipped with a LaB6 cathode, a Gatan Orius 833 CCD camera, and a homemade automatic orientation analysis software – Euclid's Phantasies (EP) (Fundenberger et al., 2003). The TEM thin foil samples were prepared first by mechanical thinning to a thickness of about 70 μm and then by electro polishing to perforation at -35°C in a solution of 5% perchloric acid in ethanol at a voltage of 35V, using a Struers Tenupol-5 twin-jet electropolisher.

The isothermal compressions were also performed *in-situ* under neutron diffraction measurements at 973 K to the as β quenched specimens with the dimensions of Φ5mm x 10mm, using the rotatable multifunctional (tension/compression/torsion) loading frame incorporated in the STRESS-SPEC instrument. The loading frame is also integrated with a clip-on extensometer and a home-made inductive heating system. The specimens were heated in air to 973 K at a rate of 50K/s, then isothermally compressed to a true strain of 0.35 and finally cooled with compressed air. The neutron diffraction measurements were performed using the neutron diffractometer STRESS-SPEC located at a thermal beam port of FRM-II (Garching, Germany). The Ge (311) monochromator was selected to reflect neutrons with a wavelength of 1.7076 Å. The $\{110\}_\beta$ diffraction peak (corresponding to β phase), $\{0002\}_\alpha$ and $\{10\bar{1}1\}_\alpha$ diffraction peaks (corresponding to α phase) were recorded at the detector position of $2\theta=42°$ with a window of 15°. The diffraction patterns were collected *in-situ* during the heating, isothermal compression and cooling processes each at every 20 seconds.

The $\{110\}_\beta$ pole figure of the un-deformed specimen (as-solution treated or β quenched) and the $\{110\}_\beta$ and $\{0002\}_\alpha$ pole figures of the same specimen after the deformation were measured ex-situ to find out the favorable diffraction measurement geometry allowing recording the reflections of the very first precipitation of the intragranular α precipitates according to our recent work on β to α transformation under compression (Hua et al., 2018). The experimental setup is detailed in Appendix. The gauge volume of the specimens for the pole figure measurements was Φ5 × 10 mm. The software StressTextureCalculator (STeCa) (Randau et al., 2011) was used to extract the diffraction patterns.

3. Results and discussion

3.1 Initial β quenched microstructure and lattice constants of the corresponding phases at deformation temperature

Fig. 1 shows the EBSD orientation micrograph of the as-solution-treated microstructure of the Ti-7333 with the corresponding correlated disorientation angle distribution. It is seen that the alloy is composed of the single β phase in a form of equiaxed grains with an average size of about 119 ± 76 μm (Fig. 1(a)). Here the standard deviation indicates the size distribution spread but not the experimental error. The β grains are rather randomly oriented than textured, as shown by the correlated disorientation angle distribution (Fig. 1(b)). Such a microstructure is typical of solution treated or β quenched metastable β Ti alloys (Hua et al., 2017; Lai et al., 2018). The initial texture is represented by the $\{110\}_\beta$ pole figure in Fig. 1(c). It is

seen that the texture is globally random. The uneven distribution of the pole densities is from two factors. The first one is that the grain sizes of the β grains are large. The total number of grains in the measured volume is relatively small (less than 1500). Thus not all the orientation space is occupied by orientations. The second is that the grain sizes are not homogeneous (with a spread of ± 76 μm). Thus the individually located higher pole densities are from large grains. According to the variant selection criteria revealed by our previous results (Hua et al., 2018), The $\{110\}_\beta$ planes that can be the Burgers orientation relationship plane for the selected intragranular α precipitates during deformation can be determined. Thus the orientation of the specimen with respect to the incident beam and the detector can be figured out, as detailed in Appendix. In Fig. 1(b), the $\{110\}_\beta$ reflection used to monitor the phase transformation for intragranular α is indicated with the black square.

At the deformation temperature (973K) that is lower than T_β (1123K), the β to α phase transformation happened. The lattice constants of the two phases at 973K measured previously (Hua et al., 2018) are listed in Table 1. These lattice constants will be used to analyze the lattice deformation during the β to α phase transformation.

Table.1 The lattice constants of β and α phases in Ti-7333 alloy at 973 K (Hua et al., 2018).

Phase	Lattice structure	Lattice constants
β	BCC	a=3.2471 Å
α	HCP	a=2.9340 Å; c=4.6795 Å

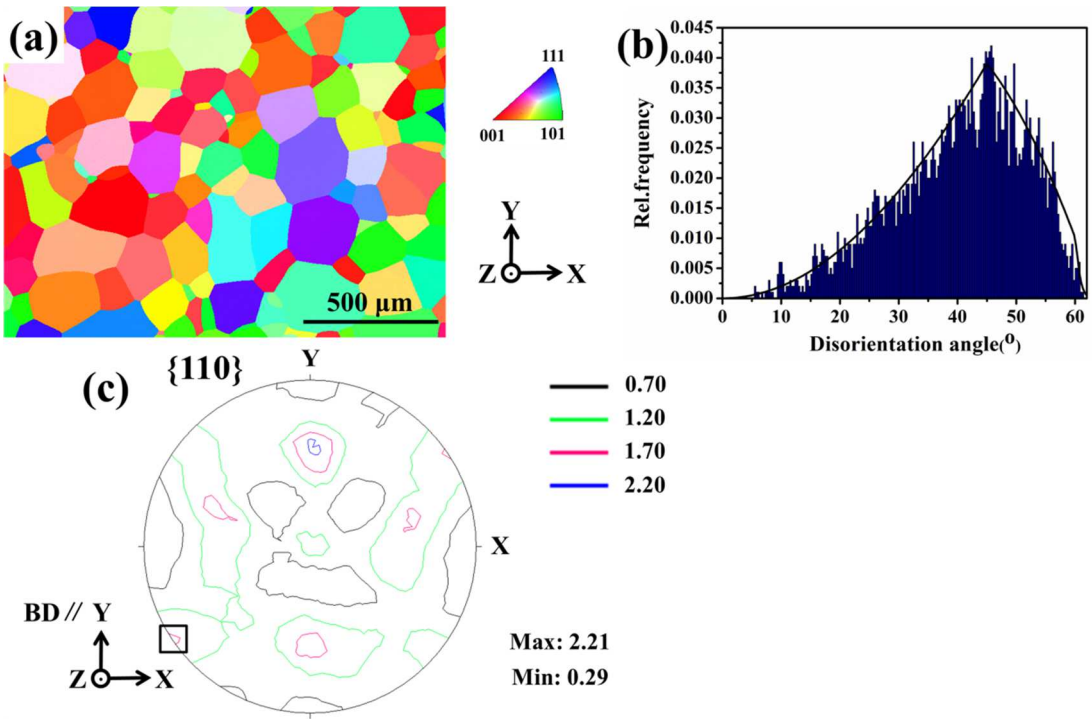

Fig.1 (a) SEM-EBSD Y axis inverse pole figure (IPF) micrograph of the solution-treated Ti-7333 alloy (Y//axial axis of the cylindrical specimen); **(b)** the corresponding correlated disorientation angle distribution, where the disorientation angle distribution of theoretical randomly oriented cubic polycrystals is represented with line profile; **(c)** $\{110\}_{\beta}$ pole figure measured by neutron diffraction. The $\{110\}_{\beta}$ reflection used to monitor the phase transformation for intragranular α is indicated with the black square.

3.2 Mechanical behavior

Figure 2 shows the true stress-strain curve and the corresponding work hardening rate curve of one specimen unidirectionally compressed to the true strain of 0.35. From the true stress-strain (σ-ε) curve (in red in Fig. 2), it is seen that, as a function of the strain, the stress starts with a linear part, corresponding to an elastic deformation, then undergoes a sudden drop from the peak, the so-called discontinuous yielding, and finally reaches a steady-state. Such a stress-strain behavior of the present alloy is typical of isothermally compressed metastable β Ti alloys (Mandal et al., 2017). The work hardening rate ($d\sigma/d\varepsilon$) (in blue in Fig. 2) well reveals the 3 stages of the present deformation. Thus we labeled them State I (elastic deformation), II (discontinuous yielding) and III (steady-state), as indicated in Fig. 2. To further reveal the origins of the three deformation stages, we will focus ourselves only on the evolution of the deformation microstructure.

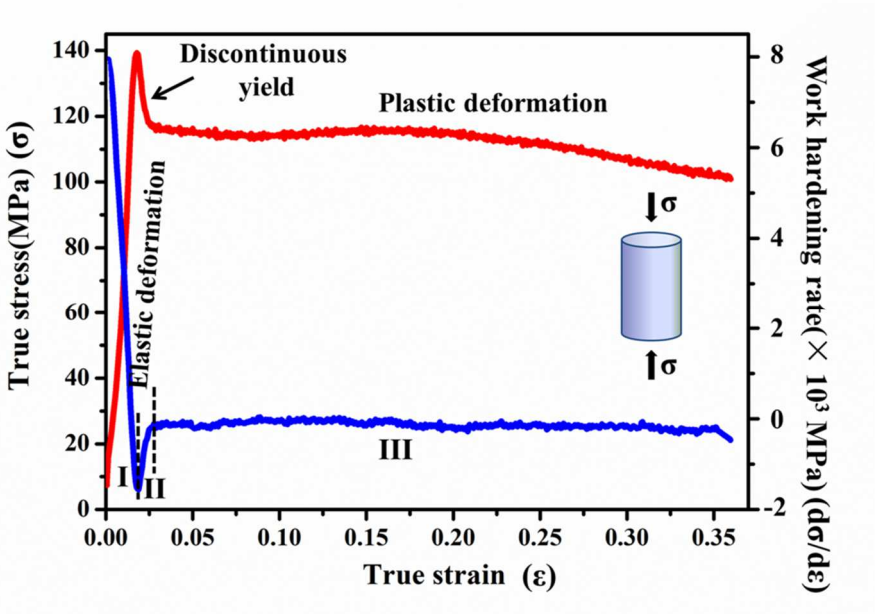

Fig. 2 Stress-strain (σ-ε) curve (in red) of the Ti-7333 alloy compressed at 973K to the strain of 0.35 and the corresponding work hardening rate-strain (dσ/dε-ε) curve (in blue).

3.3 Correlation between microstructure and deformation behavior

3.3.1 Stage I and II

Fig. 3 and Fig. 5 display large scaled microstructures of specimens deformed to the true strains of 0.015 and 0.03, with the corresponding stress-strain curves. The former deformation corresponds to the strain at the peak stress just before the discontinuous yielding (Stage I), whereas the latter to the end position of the discontinuous yielding (Stage II). It is seen that when the specimen was deformed to 0.015, the β grains still retain the equiaxed shape and there is no obvious grain growth. The average grain size is about 121 ± 66 μm (Fig. 3(a)) (as noted above, the standard deviation indicates rather the size spread than experimental error). A close examination revealed that a large amount of α phase is present along the grain boundaries of the β phase but no α phase is spotted in the β grain interiors (Fig. 3(b)). This evidences that the grain boundary α precipitates (α_{GB}) were already formed before the end of the Stage I deformation, but the intragranular α precipitates were not yet formed till then. According to the presence and the morphology of the grain boundary α precipitates (α_{GB}), the β grain boundaries can be categorized into 3 types: with continuous α_{GB}, with discontinuous α_{GB} and without α_{GB}, as shown in Fig. 3(b). Statistical analysis made on a total area of 2 × 1 mm^2 revealed that 92% of the length of the β grain boundaries is covered by α precipitates. The majority part of the boundaries are covered by continuous α (89%), whereas only a very minor portion of the β grain boundaries by discontinuous α (3%), as shown in Fig. 6. This demonstrates that before the end of the first stage of the deformation (Stage I) the β to α phase

transformation happened intensively on the β grain boundaries. Almost all the boundary regions were transformed to the α phase. As the α phase is harder than the β phase, the formation of the α_{GB} strengthens the β grain boundaries.

From the Grain Gravity Center Referenced Orientation Deviation (GGCROD) analysis result displayed in Fig. 3(c) (Note: the GGCROD map is represented with the disorientation angle of each EBSD measurement pixel within each recognized grain referenced to the orientation of the pixel at the grain gravity center), one can find that in many β grain boundary regions, especially where near triple junctions, the orientations of these regions are deviated from those of the corresponding grain gravity centers. A deviation as large as 1-2° can be detected, as shown in the zoomed GGCROD map in Fig. 3(c). This suggests that plastic deformation already started in the linear part of the stress-strain curve. Further TEM examination in the deformed β grain boundary regions at the strain of 0.015 revealed that such regions contain large amounts of dislocations, organizing into dislocation bands (slip bands), as shown in Fig. 4(a). Further determination using the trace analysis method (Zhang et al., 2011) demonstrated that most of the dislocations are of $\{110\}_\beta<1\bar{1}1>_\beta$ edge type. Such dislocations are mobile. Some dislocations present at the phase boundaries are with the one part of the lines in the β phase and the other part in the α phase, as shown by one example in Fig. 4(b1). Detailed crystallographic analysis showed that the α_{GB} respects the Burgers orientation relationship (BOR) with the β grain, β1, as demonstrated with the BOR plane and direction pole figures in Fig. 4(b) (the OR planes and directions are outlined with the black rectangles), with some angular

deviations (about 1.78° between the OR planes and about 2.97° between the OR directions). In fact, the BOR plane ($\{110\}_\beta$ /$\{0001\}_\alpha$) and BOR direction ($\langle 1\bar{1}1\rangle_\beta$ /$\langle 11\bar{2}0\rangle_\alpha$ in the two phases belong to their slip systems. Further dislocation line orientation analysis demonstrated that the dislocations in β1 (Fig. 4(b1)) are also $\{110\}_\beta$ $\langle 1\bar{1}1\rangle_\beta$ edge type with the line vector parallel to $\langle 1\bar{1}\bar{2}\rangle_\beta$. The dislocation in the α_{GB} is edge type basal ($\{0001\}_\alpha\langle 11\bar{2}0\rangle_\alpha$) dislocation with dislocation lines parallel to the $\langle 10\bar{1}0\rangle_\alpha$, as shown in the $\langle 1\bar{1}\bar{2}\rangle_\beta$ and $\langle 10\bar{1}0\rangle_\alpha$ pole figures in Fig. 4(b2), where the orange lines indicate the projection of the dislocation lines. These dislocations lie just on the BOR planes in the two phases. Such a result could be from two processes. The one could be that the two phases had reacted independently with the external loading and the slip systems coincident with the BOR systems had been activated simultaneously. The other could be that dislocations had first formed on the BOR system in the β phase and the concentrated stress accumulated at the phase boundaries when they moved to the boundary regions activated the BOR system in the α phase. The slip transfer conditions have been theoretically analyzed in detailed by Joseph et al., 2018 and Zheng et al., 2018. The formation of the large amount of dislocations near the grain boundary regions evidences that the plastic deformation indeed started in the linear part of the deformation, before the yielding point. To further clarify the possible starting point of the plastic deformation in Stage I, we calculated the Young's modulus of the alloy using the linear part of the curve in Fig. 3(d). The obtained value is about 16 GPa. By comparing the slope of the curve in Stage I with the determined Young's modulus, as shown by Fig. 3(d)-inset, we found

that the curve started to deviate from the linear relation at the strain of about 0.013. Thus the detectable macroscopic plastic deformation happened at the late state of Stage I.

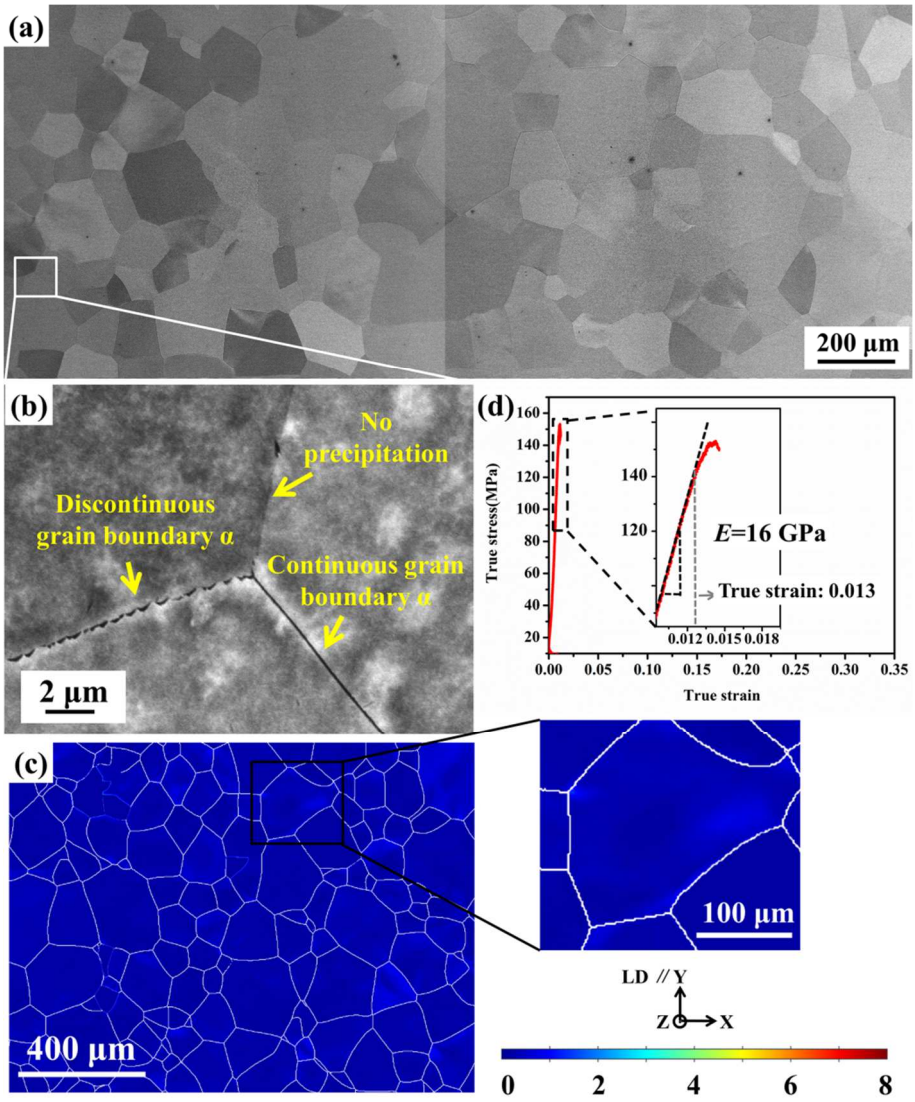

Fig. 3 SEM-BSE and EBSD micrographs of the Ti-7333 deformed at 973 K to the true strain of 0.015 (loading direction is parallel to Y axis), showing **(a)** the global microstructure, **(b)** β grain boundaries with continuous and discontinuous α precipitates, and without α precipitates, **(c)** micrograph of Grain Gravity Center Referenced Orientation Deviation (GGCROD) with one example area magnified to show the GGCROD and **(d)** the corresponding deformation stress-strain curve corresponding to Stage I. The inset shows the determined Young's modulus and the onset of the stress-strain curve deviating from the linear relation.

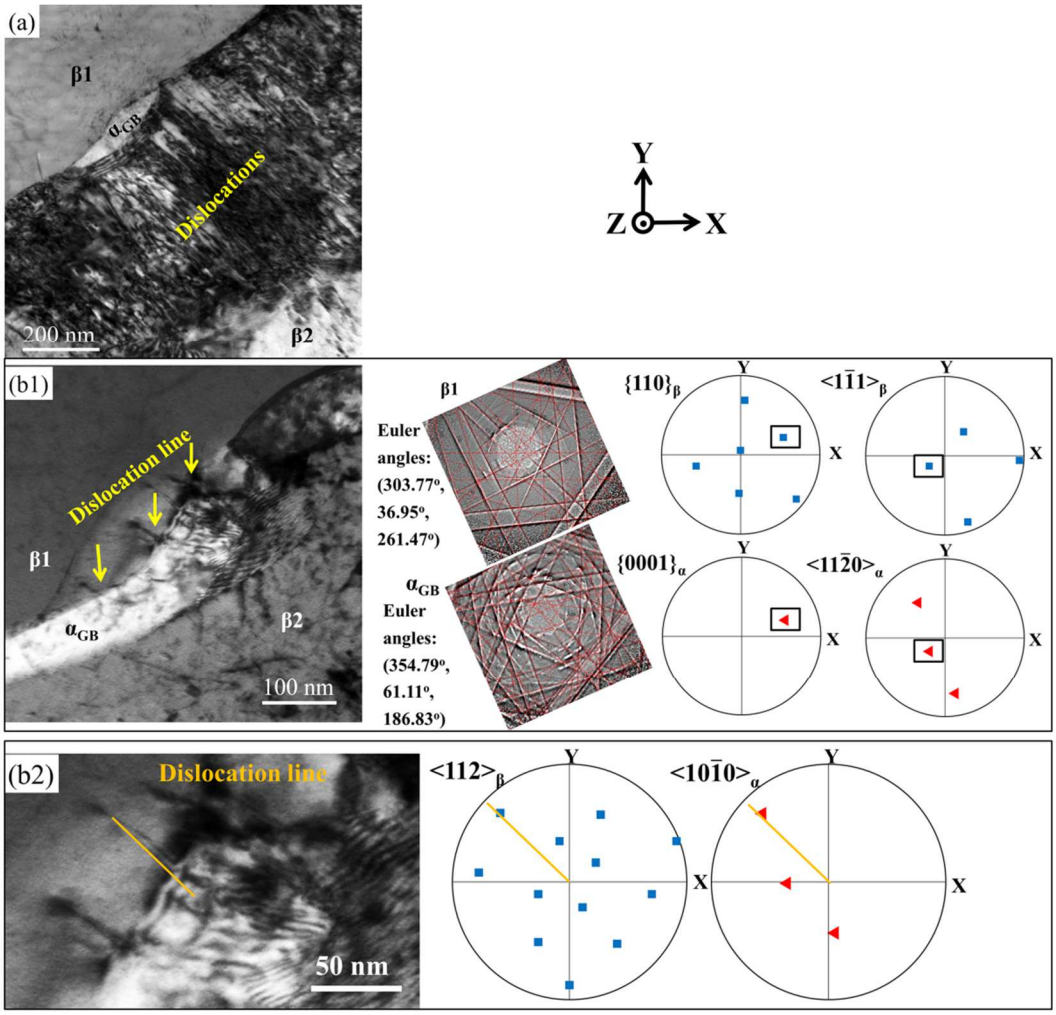

Fig. 4 TEM bright field micrographs of Ti-7333 alloy after being deformed at 973 K to 0.015, showing **(a)** dislocation band along α_{GB}; **(b)** dislocations cutting through the α_{GB}. In **(b1),** example Kikuchi line patterns from grain β1 and α_{GB} are displayed, together with the BOR plane and direction pole figures. The common poles from the two phases are framed. **(b2)** shows the magnified image the dislocation lines in the two phases (indicated with the orange line), together with the line direction pole figures.

When the specimen was deformed to the true strain of 0.03, the end point of the discontinuous yielding (the end of Stage II), the β grains are still in equiaxed shape but certain grains underwent further grain growth (Fig. 5(a)). Concerning the β to α transformation, no intragranular α precipitates were observed and the amount of α_{GB} stays almost unchanged. Still 92% of the length of the β grain boundaries is covered by the α_{GB}, as shown in Fig. 6. However, the amount of discontinuous α_{GB} is increased from 3% at the strain of 0.015 to 14% to the strain of 0.03, indicating that more α_{GB} becomes discontinuous or fragmented. Such fragmentation of the α_{GB} should be related to the cut-through of the dislocations, as already happened at the strain of 0.015 (Fig. 4(b)). As more than 90% of the boundary length is covered by α_{GB}, the movement of the dislocations across β grain boundaries has to cut through the α_{GB}, and as a result, the continuous α_{GB} is fragmented. Clearly, the fragmentation of the continuous α_{GB} weakens the strengthening effect of the α_{GB} to the β grain boundaries. Furthermore, almost all the β grain boundary regions are deformed, as evidenced by the GGCROD micrograph in Fig. 5(c). The orientations of the β regions near the grain boundaries are largely deviated (2.5°-5°) from those of their gravity center, inferring the intensive formation of dislocations. Therefore the rapid stress drop during the discontinuous yielding in Stage II should be related to the fragmentation of the α_{GB} and the formation of the dislocations in a collective avalanche-like way near the β grain boundary areas. The present result provides more detailed experimental evidences to the assertion that the discontinuous yielding in Ti alloys is from the formation of the large quantities of mobile dislocations. Moreover, the fragmentation

of the α_{GB} softened the material at β grain boundary regions and thus contributes also to the yielding.

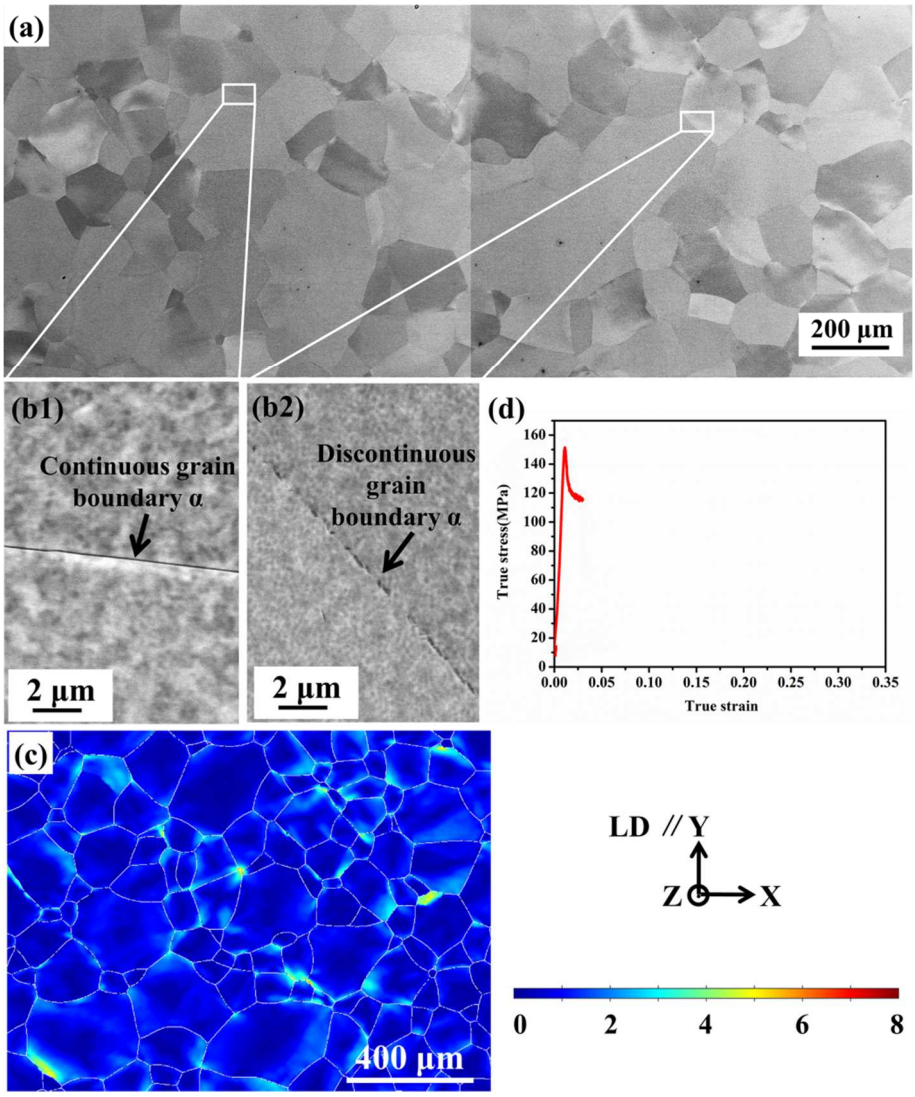

Fig. 5 SEM-BSE and EBSD micrographs of the Ti-7333 deformed at 973 K to the true strain of 0.03 (loading direction is parallel to Y axis), showing **(a)** the global microstructure, **(b1)** and **(b2)** the β grain boundaries with continuous and discontinuous α precipitates and without α precipitates, **(c)** micrograph of Grain Gravity Center Referenced Orientation Deviation (GGCROD) and **(d)** the corresponding deformation stress-strain curve corresponding to Stage II.

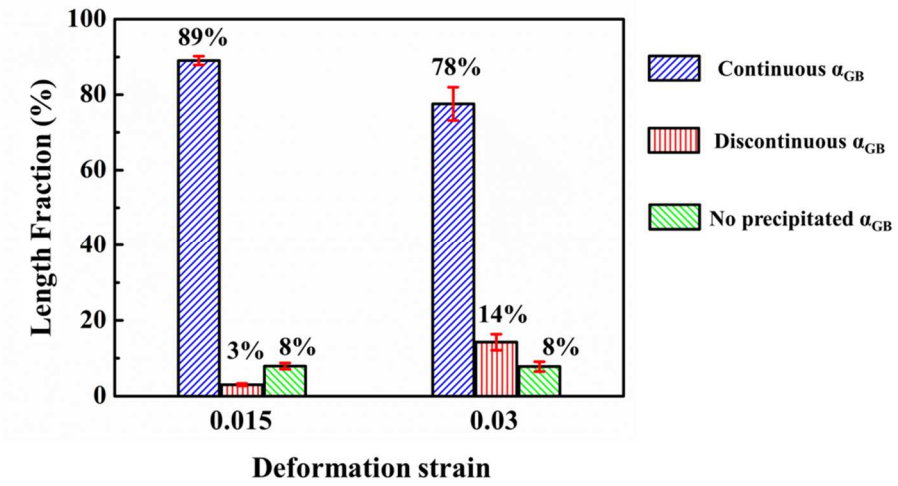

Fig. 6 Length percentages of β grain boundaries with continuous α_{GB}, with discontinuous α_{GB} and without α_{GB} in the specimens deformed to the respective strains of 0.015 and 0.03. The data are collected from an area of 2×1 mm^2.

3.3.2 Stage III

Fig. 7 shows the neutron diffraction intensity evolutions of the $\{110\}_\beta$ reflection from the β phase and the $\{0002\}_\alpha$ reflection from the α phase during the compression. It should be mentioned that the diffraction intensity of the α phase is from the intragranular α, as the formation of the α_{GB} ended before the end of Stage I (at the strain of about 0.015) and no α intensity was detected during this period, as seen in Fig. 7(a). This is due to the fact that α_{GB} is very thin and distributed along the randomly oriented and coarse β grain boundaries. Thus the amount of α_{GB} is not sufficient to produced detectable diffraction intensity. Moreover, during the *in-situ* neutron diffraction measurement, the detector position was fixed, not allowing detecting all the possible reflections from the α_{GB}. Therefore, the diffracted intensity from the α_{GB} may be largely submerged in the background noise. The experimental setup allowing such detection is detailed in Appendix. It is seen that the intragranular α started to precipitate with detectable amount at the strain of 0.14 (corresponding to 140s of the isothermal holding and in the middle of the steady stress-strain state, Stage III). After the transformation, the intensity of the diffraction peak of the α phase presents a very slow increase till the strain of 0.2 and stays stable afterwards, meaning that the transformation started very rapidly at the beginning and finished at strains about 0.2. Correspondingly in the stress-strain curve, the stress increases very slightly at 0.14 but decreases from 0.2. The slight upturning of the stress-strain curve in Stage III is coincident with the formation of the intragranular α precipitates.

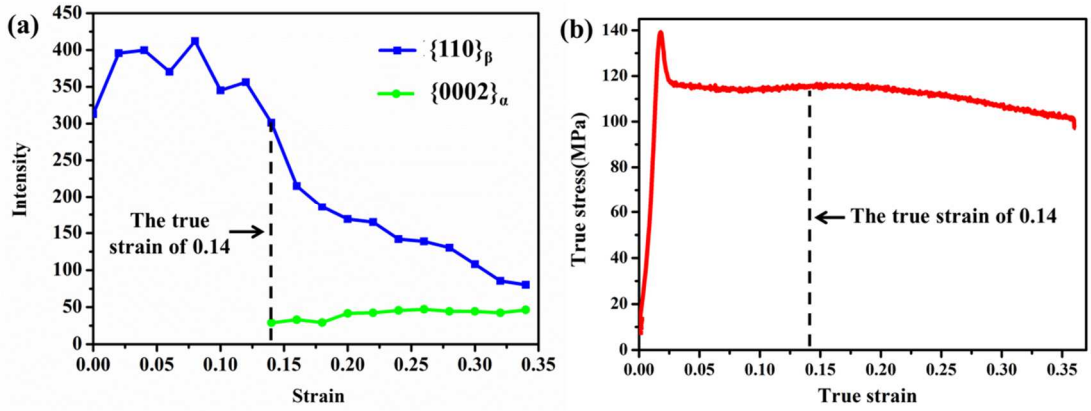

Fig. 7 Evolution of the diffraction intensities of the $\{110\}_\beta$ reflection of the β phase and the $\{0002\}_\alpha$ reflection of the α phase during the isothermal compression .

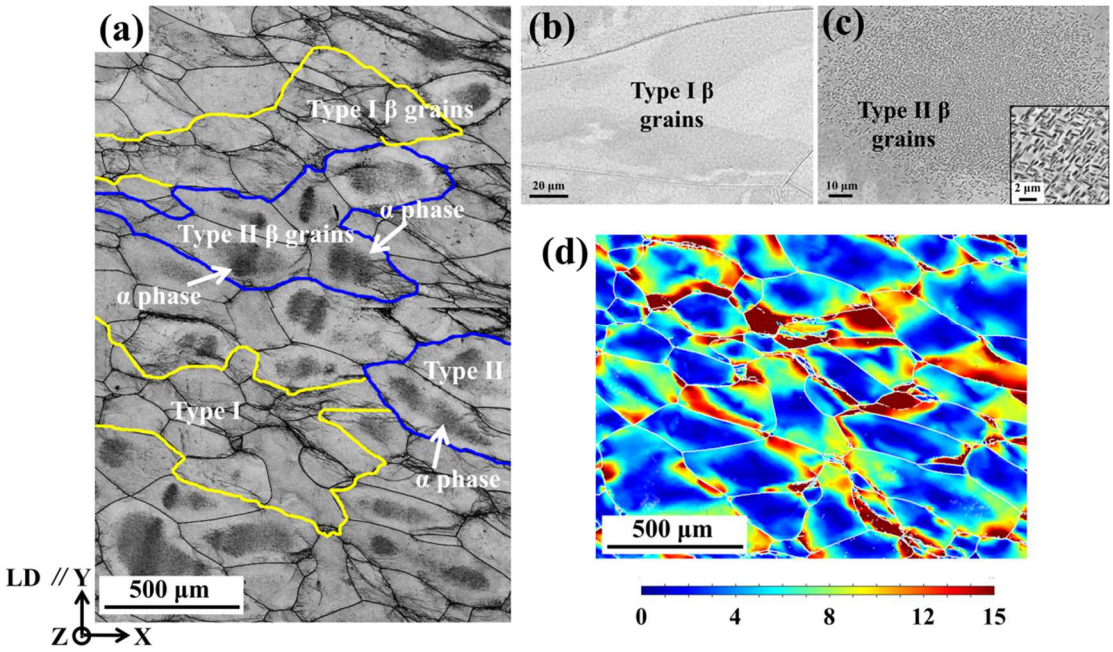

Fig. 8 (a) EBSD band contrast micrograph of the Ti-7333 alloy after unidirectional compression at 973 K (loading direction is parallel to Y axis) to the strain of 0.35. The β grains are in light gray and the α phase are in dark gray, as shown in the figure. The black lines represent the β grain boundaries. **(b)** A magnified BSE image showing type I β grains with few α precipitates. **(c)** A magnified BSE image showing type II β grains with α precipitates in the grain interiors. **(d)** Grain Gravity Center Referenced Orientation Deviation (GGCROD) micrograph.

Fig. 8 presents the deformed microstructures of the specimen compressed to the true strain of 0.35 corresponding to the end point of Stage III in the stress-strain curve in Fig. 2. It is seen that after the deformation to the strain of 0.35, most of the β grains are elongated in a direction either perpendicular to the compression direction or inclined, to some extent, to this direction. Furthermore, α phase is intensively precipitated in the β grains. However, the precipitation amount in different β grains is very heterogeneous. According to the precipitation amount, we further classify the β grains into two types, Type I and Type II. For the type I grains, as outlined with the yellow lines in Fig. 8(a), there appear almost no or very slight amount of α precipitates. A magnified micrograph of such grains is displayed in Fig. 8(b). However, for the type II grains, as outlined with the blue lines in Fig. 8(a), large amount of α precipitates appear in the β grains, especially in the grain interiors. A magnified micrograph of such grains is displayed in Fig. 8(c). The area percentages of the two kinds of grains were measured in a cross section area of 1.7×3 mm^2. This area cuts the whole homogeneous deformation zone in the sample. The results showed that the area percentage for the type I grains is about 54%, and that for the type II grains is about 46%. Detailed microstructural and crystallographic examination of the α precipitates in the interiors of the type II β grains revealed that the α precipitates are in plate-shape (Fig. 8(c)-insert) and respect the Burgers orientation relationship (BOR) with the surrounding β matrix. In each type II grain, only two α variants are detected and the two variants are disoriented by 90° around the $<1\ 1.38\ \overline{2.38}\ 0>_{\alpha}$, forming cross shaped clusters. Such a crystallographic character of the α precipitates was

verified in all the type II β grains in the whole cross section of the deformed zone in the sample (1.7 × 3 mm^2) and found to be reproduced in all the type II grains. Thus the results are statistically relevant. The deformation of the β grains was further analyzed, using the measured EBSD data, and represented with the micrograph of Grain Gravity Center Referenced Orientation Deviation (GGCROD), as shown in Fig. 8(d). It is seen that the most deformed regions are still located near the β grain boundaries, especially the triple junctions, with the maximum disorientation (in angle) up to 19°. Compared with the deformation situation shown in Fig. 3(c) (strain of 0.015) and in Fig. 5(c) (strain of 0.03), the deformed regions in each β grain extend from the grain boundary regions toward the grain interiors, especially in the type I β grains. For the type II grains the disoriented regions are mainly located in the "mantle" part of the β grains where almost no α precipitates appear.

Further TEM examinations revealed that in the type I β grains there exists large amount of dislocations, as shown in Fig. 9(a). The dislocations are organized in bands (as outlined with the white lines in the figure) and within each band the dislocation lines are aligned roughly in the same direction (as indicated with the orange and green lines). Orientation analysis using the acquired Kikuchi patterns from different slip bands, for example Bands 1 and 2 in Fig. 9(a), demonstrated that the slip bands are slightly disoriented (about 2°), as shown by the $<100>_\beta$ pole figure. Further determination using the method developed by our group (Zhang et al., 2011) confirmed that the dislocations are still of the $\{110\}_\beta<1\bar{1}1>_\beta$ edge type with the dislocation lines parallel to the $<1\bar{1}\bar{2}>_\beta$ direction. The dislocations in different bands

are of the same type but are crystallographic variants, as shown by the $<1\bar{1}\bar{2}>_\beta$ pole figures in Fig. 9(a), where the projections of the dislocations in Bands 1 and 2 are indicated with the consistent color lines as those in the TEM bright field micrograph. In the present work we found that such slip bands go through the entire β grains (type I). It is worth mentioning that no $\{112\}_\beta<11\bar{1}>_\beta$ dislocations were evidenced in the present alloy. The absence of this type of dislocations is consistent with what reported in the literature that the $\{112\}_\beta<11\bar{1}>_\beta$ slip system in BCC crystals are more easily activated at low deformation temperatures than at high temperatures (Rollett et al., 2017). The formation of the slip bands should be related to the temperature effect. Obviously recovery occurred intensively with the deformation. However, no recrystallized grains were detected, suggesting that there is no occurrence of recrystallization during the present compression to the strain of 0.35. In contrast, in the type II grains no dislocation bands were found existing in the zones where the α precipitates were intensively formed, as shown in Fig. 9(b), indicating that the deformation mechanisms are different in the two types of grains. In the former the deformation is controlled by dislocation activity and in the latter the deformation is accommodated mainly by phase transformation.

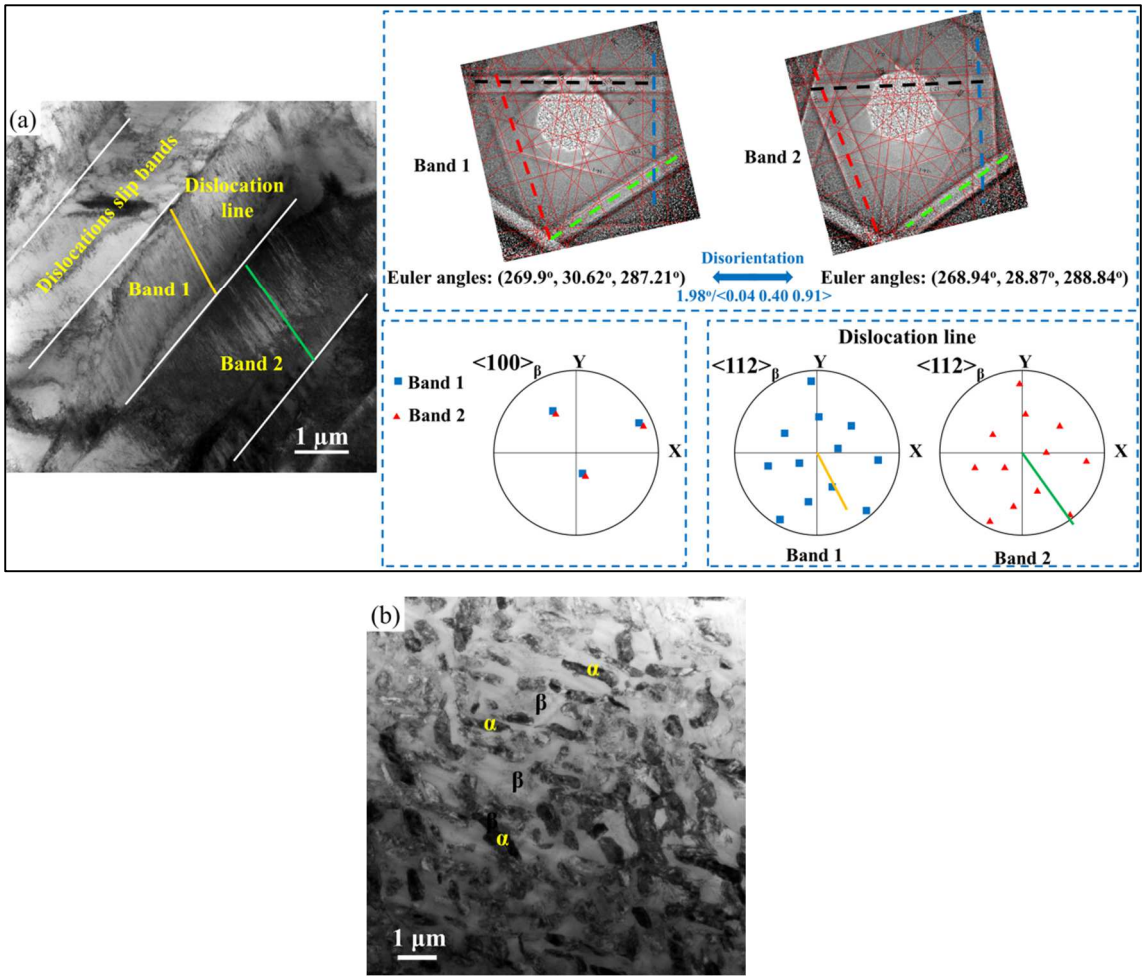

Fig. 9 TEM bright field micrographs of Ti-7333 alloy after being compressed at 973 K to the strain of 0.35, **(a)** showing the dislocations in slip bands in the type I β grains where there are almost no α precipitates and **(b)** showing the large amount of α precipitates in type II β grains. In (a), example Kikuchi line patterns from Bands 1 and 2 are displayed, together with the $<100>_{\beta}$ direction pole figure to show that the band regions are slightly disoriented. The dislocation lines in the two bands are also indicated with the $<112>_{\beta}$ direction pole figures, showing that the dislocations in the bands are of the same type but are crystallographic variants.

Obviously the two types of β grains contribute to the external deformation in different ways. For the type I grains, the contribution is made mainly by the $\{110\}_\beta\langle 1\bar{1}1\rangle_\beta$ dislocation slip. Thus their crystallographic orientations ensure the $\{110\}_\beta\langle 1\bar{1}1\rangle_\beta$ slip system to be in the favorable activation position to the external load. For the type II β grains, the contribution is mainly made by the lattice deformation from the β to α transformation, as the structure transformation involves a large shear in the $\{1\bar{1}\bar{2}\}_\beta\langle\bar{1}1\bar{1}\rangle_\beta$ system and some normal strain components, as shown in **Table 2**. For comparison, the displacement gradient tensor of the $\{110\}_\beta\langle 1\bar{1}1\rangle_\beta$ slip expressed in the same reference system (BOR system $i//[1\bar{1}\bar{2}]_\beta$ $j//[\bar{1}1\bar{1}]_\beta$ $k//[110]_\beta$) is also given in the table. It should mentioned that the value in the displacement gradient tensor of the $\{110\}_\beta\langle 1\bar{1}1\rangle_\beta$ slip is obtained by dividing the magnitude of the Burgers Vector (*b*) with the interplanar spacing of the $\{110\}_\beta$ slip planes in the β phase. The value is only indicative and far from the reality, as in the real case the value in the tensor is dislocation density dependent. The crystallographic orientations of the type II β grains should allow the $\{1\bar{1}\bar{2}\}_\beta\langle\bar{1}1\bar{1}\rangle_\beta$ system in the favorable position to be activated by the external load. To verify these assertions, the orientation of the two types of β grains measured from the sample area of 1.7×3 mm^2 that corresponds to the whole cross section area of the deformed zone were analyzed and represented in the orientation space (Euler angle space). Fig. 10 shows the φ_2 sections of the measured orientations of the two types of β grains and the calculated resolved shear stress of the unitary external compressive load on the respective $\{110\}_\beta\langle 1\bar{1}1\rangle_\beta$ and $\{1\bar{1}\bar{2}\}_\beta\langle\bar{1}1\bar{1}\rangle_\beta$ systems of the randomly oriented β grains (2.85 x

10^6) that are distributed in the whole orientation space. The calculated resolved shear stress of each Euler orientation is shown with the highest one among the system families. The random β orientations were generated using the algorithm proposed by Morawiec, 2003. Comparing Fig. 10(a) with Fig. 10(b), and Fig. 10(c) with Fig. 10(d), one can find that the type I β grains are indeed oriented with one of their $\{110\}_\beta\langle 1\bar{1}1\rangle_\beta$ slip systems in the favorable position for activation, i.e., the external load resolves a maximum shear stress on the system, whereas the type II β grains are oriented with one of their $\{1\bar{1}2\}_\beta\langle \bar{1}1\bar{1}\rangle_\beta$ shear systems in the favorable position for activation.

Table 2 Displacement gradient tensor of $\{110\}_\beta\langle 1\bar{1}1\rangle_\beta$ slip and that of β to α phase transformation expressed in Burgers Orientation Relationship (BOR) coordinate system: (*i.e.* $i // [1\bar{1}2]_\beta$, $j // [\bar{1}1\bar{1}]_\beta$ and $k // [110]_\beta$) .

Deformation system	Displacement gradient tensor
$\{110\}_\beta\langle 1\bar{1}1\rangle_\beta$	$\begin{pmatrix} 0 & 0 & 0 \\ 0 & 0 & \pm 0.3772 \\ 0 & 0 & 0 \end{pmatrix}$
β to α transformation	$\begin{pmatrix} -0.0416 & 0 & 0 \\ \mathbf{-0.1844} & 0.0434 & 0 \\ 0 & 0 & 0.0189 \end{pmatrix}$

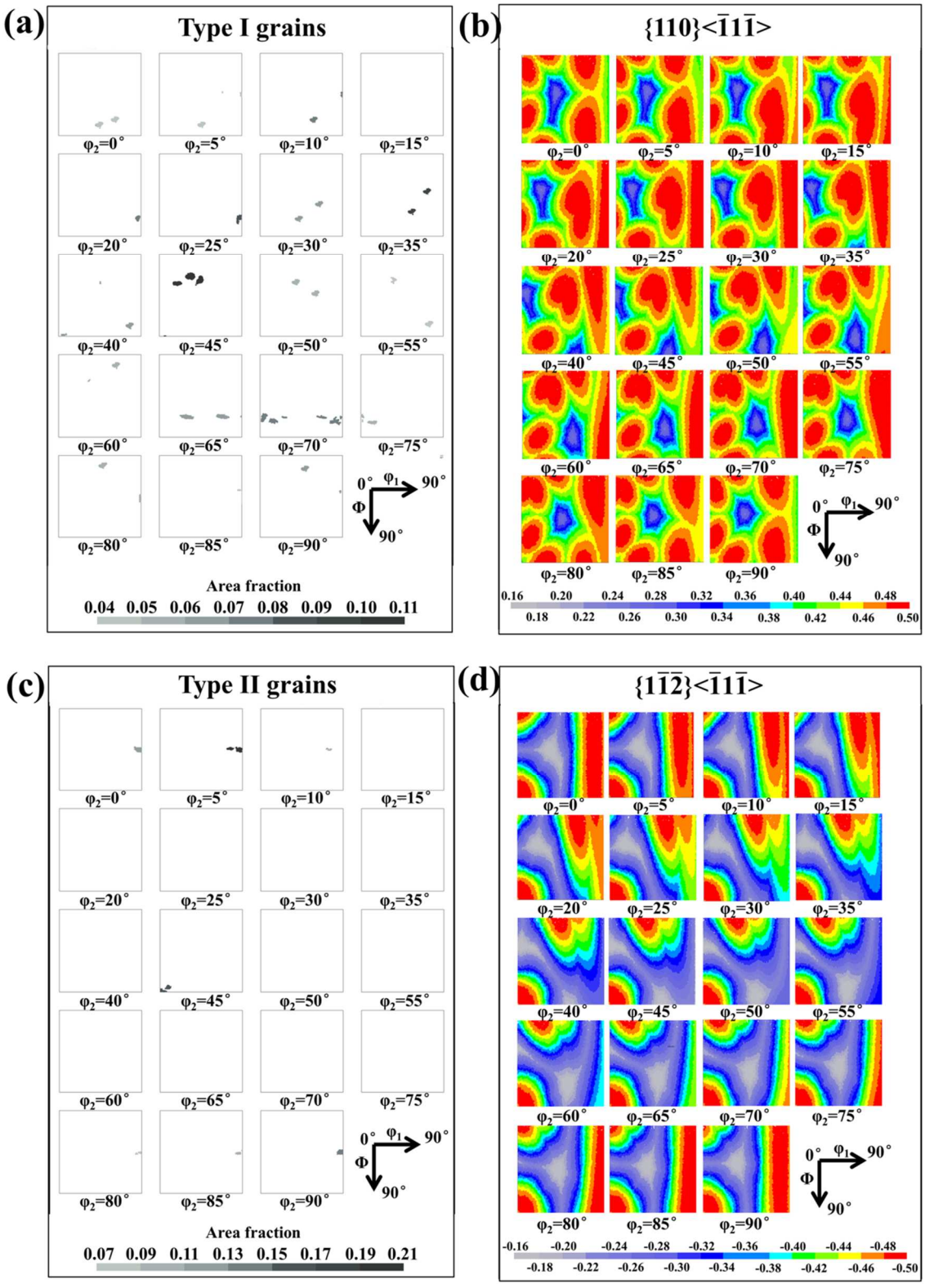

Fig. 10 (a) and **(c)** φ_2 sections of the measured orientations of the respective type I and type II β grains normalized with the total areas of the respective type of β grains and **(b)** and **(d)** calculated resolved shear stress of the unitary external compressive

load on the respective $\{110\}_\beta\langle 1\bar{1}1\rangle_\beta$ and $\{1\bar{1}\bar{2}\}_\beta\langle \bar{1}1\bar{1}\rangle_\beta$ systems of randomly oriented β grains ($2.85x10^6$) that are distributed in the whole orientation space. The resolved shear stress shown for each Euler orientation is that of the system with highest value among the shear system families considered.

To evaluate the contribution possibilities of the two deformation modes ($\{110\}_\beta\langle 1\bar{1}1\rangle_\beta$ slip and the phase transformation) of the examined β grains, the displacement gradient tensors of the lattice transformation strain from the β matrix to the two selected α variants in one example β grain having the maximum resolved shear stress for the $\{1\bar{1}\bar{2}\}_\beta\langle\bar{1}1\bar{1}\rangle_\beta$ system and those of the dislocation slip of one example β grain with the maximum absolute resolved shear stress for $\{110\}_\beta\langle 1\bar{1}1\rangle_\beta$ slip are further expressed in the sample coordinate system (X-Y-Z, as shown in the figures of the micrographs (Fig. 1, 3 , 5 and 8)) where the compression axis is parallel to Y and one example is given in **Table 3**. It should be mentioned that the tensors displayed in the table are from the systems receiving the maximum resolved shear stress. In the tensors, the ε_{22} component is very indicative for the strain of the systems contributed to the macroscopic compression. The negative ε_{22} means that the lattice deformation (either by slip or phase transformation) produces contraction in the macroscopic compression direction. It is seen that the formation of the two α variants in the type II β grain makes positive contribution to the macroscopic compression. However for the $\{110\}_\beta\langle 1\bar{1}1\rangle_\beta$ slip, it can happen in two opposite directions, the one making positive contribution to the macroscopic deformation and the other one being opposite. The opposite ones are to accommodate local deformation. The two kinds of shear systems demonstrate quite different contribution on the macroscopic deformation. For the formation of the selected intragranular α precipitates by phase transformation, the activation of the shear system ($\{1\bar{1}\bar{2}\}_\beta\langle\bar{1}1\bar{1}\rangle_\beta$ systems) is uni-directional. The deformation thus provided is compatible with the macroscopic

compression. However, for the $\{110\}_\beta\langle 1\,\bar{1}\,1\rangle_\beta$ slip, it is bi-directional. The deformation provided can either contribute to the macroscopic deformation or to the local deformation, even though it is incompatible to the macroscopic deformation.

Table 3 Displacement gradient tensors of two α precipitates in one example of type I β grain and that of $\{110\}_\beta\langle 1\bar{1}1\rangle_\beta$ slip system of one example of type II β grain expressed in the sample X-Y-Z coordinate system. The compression is along Y axis.

Precipitates No.	Displacement gradient tensor
A	$\begin{pmatrix} 0.0238 & 0.0279 & 0.0225 \\ -0.0224 & -0.0999 & -0.0812 \\ 0.0216 & 0.0962 & 0.0952 \end{pmatrix}$
B	$\begin{pmatrix} 0.0945 & -0.0757 & -0.0152 \\ 0.1010 & -0.0989 & -0.0182 \\ -0.0308 & 0.0319 & 0.0234 \end{pmatrix}$
$(0\bar{1}1)_\beta[\bar{1}\bar{1}\bar{1}]_\beta$	$\begin{pmatrix} 0.0032 & -0.0276 & 0.0211 \\ 0.0214 & -0.1824 & 0.1393 \\ 0.0275 & -0.2347 & 0.1792 \end{pmatrix}$
$(0\bar{1}1)_\beta[111]_\beta$	$\begin{pmatrix} -0.0032 & 0.0276 & -0.0211 \\ -0.0214 & 0.1824 & -0.1393 \\ -0.0275 & 0.2347 & -0.1792 \end{pmatrix}$

These results demonstrate that the steady stress-strain behavior of the alloy is rooted from the different contributions of the two types of β grains. For the type I grains, the hardening from the multiplication of the dislocations is balanced by the rearrangement of the dislocations to the soft configurations (the slip bands in the present work) through dislocation movement, as the activation energy of the dislocation slip is decreased at elevated temperatures (Gloaguen et al., 2013; Groger and Vitek, 2013). For the type II β grains, the formation of the intragranular α precipitates should strengthen the type II β grain interiors. As they form intensively

around the strain of 0.14, as shown in Fig. 7, the slight hardening shown by the stress-strain curve in Fig. 2 is due to the formation of the intragranular α precipitates in the type II β grains. With the further progress of the deformation from the strain of about 0.2, a slight but obvious softening can be seen in the stress-strain curve in Fig. 2. The softening is mainly related to the dislocation rearrangement, but not by the formed intragranular α precipitates, as they did not show any fragmentation or spheroidization until the strain of 0.35.

4. Conclusions

The deformation process of a metastable β titanium alloy with a β quenched initial microstructure under a uniaxial isothermal compression at 973 K has been thoroughly investigated by correlating the stress-strain behavior with the microstructure evolution in multiscale. The isothermal compression of the present Ti-7333 alloy can be categorized into three typical stages, e.g., a linear state (Stage I), a discontinuous yielding (Stage II) and a steady-state (Stage III). For Stage I, the β to α phase transformation happened intensively along the β grain boundaries before and during the deformation. More than 90% of the boundaries are occupied by α_{GB}. The linear behavior of the alloy started to deviate from the Young's modulus at the late stage, indicating the onset of plastic deformation. The behavior results from the dislocation slip in the β grain boundary regions. For the discontinuous yielding, the drastic drop of the stress is originated from the fragmentation of the α_{GB} and the further formation of dislocations in a collective avalanche-like way in the β grain

boundary regions. For the steady-state stage, the deformation behavior of the β grains is further diversified into two types, i.e., type I having their $\{110\}_\beta\langle 1\bar{1}1\rangle_\beta$ slip system in the favorable orientation with respect to the external compressive load and type II with their $\{1\bar{1}\bar{2}\}_\beta\langle\bar{1}1\bar{1}\rangle_\beta$ system in the favorable orientation. Thus for the type I β grains the deformation progresses through the formation of $\{110\}_\beta\langle 1\ \bar{1}\ 1\rangle_\beta$ dislocations counter-balanced by the arrangement of the formed dislocations into slip bands, whereas for the type II β grains the deformation is realized by the intensive formation of intragranular α precipitates that is characterized by a large shear strain in $\{1\bar{1}\bar{2}\}_\beta\langle\bar{1}1\bar{1}\rangle_\beta$ system accompanied by some small lattice distortions. This evidenced that the phase transformation serves as another kind of deformation mechanism for crystal plasticity. The present work provides new information of orientation dependent deformation mechanisms of metastable β titanium alloys, especially on the contribution of the phase transformation to the overall deformation behavior and offers detailed experimental data that can be useful for the simulation of the mechanical behavior of metastable β titanium alloys.

Appendix

Experimental setup of the *in-situ* neutron diffraction measurement to detect the intragranular α precipitation

Our previous results concerning the variant selection of the intragranular α precipitates during the similar hot compression (Hua et al., 2018) indicated that the β to α phase transformation followed the Burgers orientation relationship (BOR), i.e.,

$\{110\}_\beta$//$\{0001\}_\alpha$ and $\langle\bar{1}1\bar{1}\rangle_\beta$//$\langle11\bar{2}0\rangle_\alpha$. Only the intragranular α variants having the initial $\{1\bar{1}\bar{2}\}_\beta\langle\bar{1}1\bar{1}\rangle_\beta$ shear system of the parent β grain at the favorable orientation with respect to the external load were selected. With the atomic correspondences between the two phases, as shown in Fig. A1(a), the geometrical relation between the shear system for phase transformation ($\{1\bar{1}\bar{2}\}_\beta\langle\bar{1}1\bar{1}\rangle_\beta$ shaded with the yellow lines in the figure) and the BOR system (shaded with the green lines in the figure) can be figured out. The shear plane is perpendicular to the BOR plane, and the two planes share one $\langle\bar{1}1\bar{1}\rangle_\beta$ direction that serves, on the one hand, as the shear direction and, on the other hand, as the BOR direction. As the α variant corresponding to the $\{1\bar{1}\bar{2}\}_\beta\langle\bar{1}1\bar{1}\rangle_\beta$ shear system that receives the maximum resolved shear stress from the external load can be selected, the orientation of its BOR plane with respect to the external load can be deduced, as shown in Fig. A1(b). In the ideal case, the load direction lies on the BOR plane. Since the interplanar spacing of $\{110\}_\beta$ and $\{0002\}_\alpha$ are d_{110}=4.625 Å (2θ=43.34° when λ=1.7076 Å) and d_{0002}=4.679 Å (2θ=42.57°), respectively, the two reflections can be detected simultaneously with the 2D detector (with a window of 15°) set at 2θ=42°.

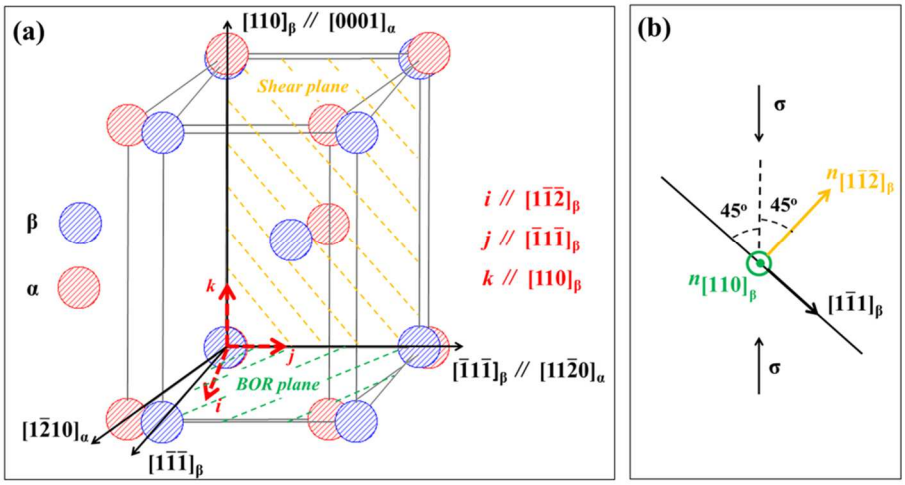

Fig. A1 (a) Atomic correspondences between the β and the α phase under the Burgers orientation relationship (BOR), where the transformation shear plane is shaded with the yellow lines and the BOR plane with the green lines; **(b)** geometrical relation between the BOR plane normal (in green) and the shear plane normal (in yellow) for the selected intragranular α variant under the compressive load σ. The shear system for its formation is in the ideal orientation to receive highest resolved shear stress from the external load.

Under such a geometrical configuration, we measured the $\{110\}_\beta$ pole figure of the initial β microstructure at the room temperature, as shown in Fig. A2(a). The load is parallel to the Z axis that is located at the center of the pole figure. According to the above deduction, the $\{110\}_\beta$ planes located at the outer circle of the pole figure could be the BOR planes for the selected intragranular α precipitates. Thus we set the geometrical configuration of the loading axis, the incident beam and the 2D detector of the *in-situ* neutron diffraction experiment to allow detecting the highest $\{110\}_\beta$ peak, as highlighted with the black frame in the pole figure in Fig. A2(a). After the sample was deformed to the true strain of 0.35, we measure the $\{0002\}_\alpha$ pole figure of the same sample under the same sample orientation with respect to the incident beam and the detector. The $\{0002\}_\alpha$ pole figure is shown in Fig. A2(b). It is seen that the highest $\{0002\}_\alpha$ pole density well correlates to the high $\{110\}_\beta$ pole density in Fig. A2(a). This result verified our neutron diffraction setup to detect the formation of the intragranular α precipitates and further confirmed the variant selection criteria that we worked out previously (Hua et al., 2018).

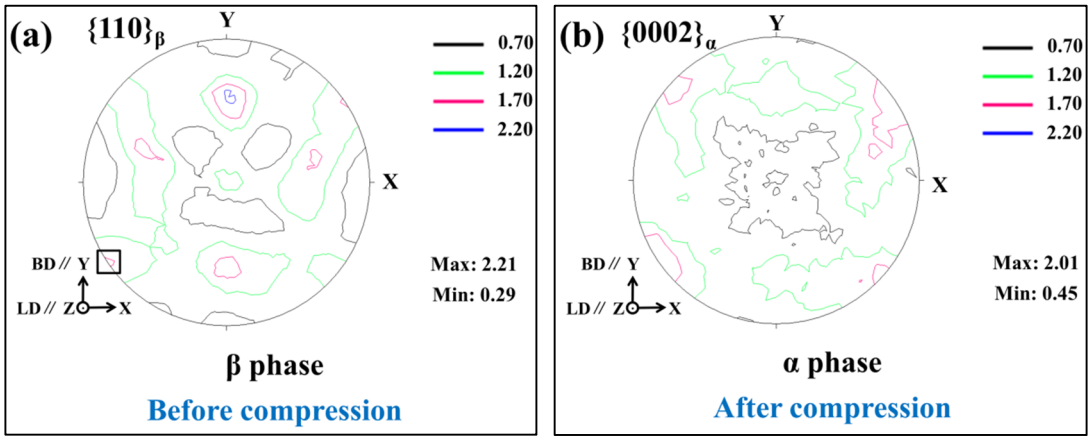

Fig. A2 (a) $\{110\}_{\beta}$ pole figure measured by neutron diffraction at room temperature before the hot compression; **(b)** $\{0002\}_{\alpha}$ pole figure measured after the hot compression. The black frame in **(a)** indicates the $\{110\}_{\beta}$ peak used to detect the formation of the intragranular α precipitates during *in-situ* neutron diffraction measurement.

Acknowledgements

This work was supported by the Major State Research Development Program of China under Grant Nos. 2016YFB0701303 and 2016YFB0701305, the Program de Recherche Conjoint CNRS-NSFC under the Grant No. PRC1475, and the National Natural Science Foundation of China under Grant No. 51711530151. This work is based upon experiments performed at the STRESS-SPEC instrument operated by HZG and FRM II at the Heinz Maier-Leibnitz Zentrum (MLZ), Garching, Germany. The authors gratefully acknowledge the financial support provided by HZG and FRM II to perform the neutron scattering measurements at the Heinz Maier-Leibnitz Zentrum (MLZ), Garching, Germany. Ke Hua is grateful to the China Scholarship Council for the financial support for his Ph.D study in France.

References

Beausir, B., Fundenberger, J.J., 2017. Analysis Tools for Electron and X-ray diffraction, ATEX software. http://www.atex-software.eu.

Bohemen, S.V., Kamp, A., Petrov, R.H., Kestens, L.A.I., Sietsma, J., 2008. Nucleation and variant selection of secondary α plates in a β Ti alloy. Acta Mater. 56, 5907-5914.

Bonisch, M. Panigrahi, A., Stoica, M., Calin, M., Ahrens, E., Zehetbauer, M., Skrotzki, W., Eckert, J., 2017. Giant thermal expansion and α-precipitation pathways in Ti-alloys. Nat. Commun. 8, 1429.

Boyer, R.R., 2010. Attributes, characteristics, and applications of titanium and its

alloys. JOM 62, 21-24.

Eyckens, P., Mulder, H., Gawad, J., Vegter, H., Roose, D., Boogaard, T., Bael, A.V., Houtte, P.V., 2015. The prediction of differential hardening behaviour of steels by multi-scale crystal plasticity modelling. Int. J. Plast. 73, 119-141.

Fujita, N., Ishikawa, N., Roters, F., Tasan, C.C., Raabe, D., 2018. Experimental–numerical study on strain and stress partitioning in bainitic steels with martensite–austenite constituents. Int. J. Plast. 104, 39-53.

Fundenberger, J.J., Morawiec, A., Bouzy, E., Lecomte, J.S., 2003. Polycrystal orientation maps from TEM. Ultramicroscopy 96, 127-137.

Furuhara, T., Poorganji, B., Abe, H., Maki, T., 2007. Dynamic recovery and recrystallization in titanium alloys by hot deformation. JOM 59, 64-67.

Gloaguen, D., Oum, G., Legrand, V., Fajoui, J., Branchu, S., 2013. Experimental and theoretical studies of intergranular strain in an alpha titanium alloy during plastic deformation. Acta Mater. 61, 5779-5790.

Groger, R., Vitek, V., 2013. Stress dependence of the Peierls barrier of 1/2< 1 1 1> screw dislocations in bcc metals. Acta Mater. 61, 6362-6371.

Hua, K., Zhang, Y., Kou, H., Li, J., Gan, W., Fundenberger, J.J., Esling C., 2017. Composite structure of α phase in metastable β Ti alloys induced by lattice strain during β to α phase transformation. Acta Mater. 132, 307-326.

Hua, K., Zhang, Y., Gan, W., Kou, H., Li, J., Esling, C., 2018. Correlation between imposed deformation and transformation lattice strain on α variant selection in a metastable β-Ti alloy under isothermal compression. Acta Mater. 161, 150-160.

Jing, L., Fu, R., Wang, Y., Qiu, L., Yan, B., 2017. Discontinuous yielding behavior and microstructure evolution during hot deformation of TC11 alloy. Mater. Sci. Eng. A 704, 434-439.

Johnston, W.G., Gilman, J.J., 1959. Dislocation velocities, dislocation densities, and plastic flow in lithium fluoride crystals. J. Appl. Phys. 30, 129-144.

Jonas, J.J., Heritier, B., Luton, M.J., 1979. Anneal hardening and flow softening in beta zirconium niobium alloys. Met. Trans. A. 10, 611-620.

Jonas, J.J., Aranas, C., Fall, A., Jahazi, M., 2017. Transformation softening in three titanium alloys. Mater. Des. 113, 305–310.

Jones, N.G., Dashwood, R.J., Dye, D., Jackson, M., 2008. Thermomechanical processing of Ti–5Al–5Mo–5V–3Cr. Mater. Sci. Eng. A 490, 369-377.

Jones, N.G., Dashwood, R.J., Dye, D., Jackson, M., 2009. The flow behavior and microstructural evolution of Ti-5Al-5Mo-5V-3Cr during subtransus isothermal forging. Metall. Mater. Trans. A 40, 1944-1954.

Joseph, S., Bantounas, I., Lindley, T.C., Dye, D., 2018. Slip transfer and deformation structures resulting from the low cycle fatigue of near-alpha titanium alloy Ti-6242Si. Int. J. Plast. 100, 90-103.

Kanjarla, A.K., Houtte, P.V., Delannay, L., 2010. Assessment of plastic heterogeneity in grain interaction models using crystal plasticity finite element method. Int. J. Plast. 26, 1220-1233.

Kestens, L.A.I., Pirgazi, H., 2016. Texture formation in metal alloys with cubic crystal structures. Mater. Sci. Technol. 32, 1303-1315.

Khan, A.S., Suh, Y.S., Kazmi, R., 2004. Quasi-static and dynamic loading responses and constitutive modeling of titanium alloys. Int. J. Plast. 20, 2233-2248.

Khan, A.S., Kazmi, R., Farrokh, B., Zupan, M., 2007. Effect of oxygen content and microstructure on the thermo-mechanical response of three Ti–6Al–4V alloys: Experiments and modeling over a wide range of strain-rates and temperatures. Int. J. Plast. 23, 1105-1125.

Khan, A.S., Liu, J., 2016. A deformation mechanism based crystal plasticity model of ultrafine-grained/nanocrystalline FCC polycrystals. Int. J. Plast. 86, 56-69.

Koike, J., Shimoyama, Y., Ohnuma, I., Okamura, T., Kainuma, R., Ishida, K., Maruyama, K., 2000. Stress-induced phase transformation during superplastic deformation in two-phase Ti–Al–Fe alloy, Acta Mater. 48, 2059–2069.

Lai, M.J., Li, T., Raabe, D., 2018. ω phase acts as a switch between dislocation channeling and joint twinning- and transformation-induced plasticity in a metastable β titanium alloy. Acta Mater. 151, 67-77.

Liu, J., Khan, A.S., Takacs, L., Meredith, C.S., 2015. Mechanical behavior of ultrafine-grained/nanocrystalline titanium synthesized by mechanical milling plus consolidation: Experiments, modeling and simulation. Int. J. Plast. 64, 151-163.

Lütjering, G., Williams, J.C., 2007. Titanium. Springer, Berlin Heidelberg.

Mandal, S., Gockel, B.T., Balachandran, S., Banerjee, D., Rollett, A.D., 2017. Simulation of plastic deformation in Ti-5553 alloy using a self-consistent viscoplastic model. Int. J. Plast. 94, 57-73.

Matsumoto, H., Kitamura, M., Li, Y., Koizumi, Y., Chiba, A., 2014. Hot forging

characteristic of Ti–5Al–5V–5Mo–3Cr alloy with single metastable β microstructure. Mater. Sci. Eng. A 611, 337-344.

Meredith, C.S., Khan, A.S., 2012. Texture evolution and anisotropy in the thermo-mechanical response of UFG Ti processed via equal channel angular pressing. Int. J. Plast. 30, 202-217.

Morawiec, A., 2003. Orientations and Rotations. Springer, Berlin.

Ozturk, T., Rollett, A.D., 2018. Effect of microstructure on the elasto-viscoplastic deformation of dual phase titanium structures. Comput. Mech. 61, 55-70.

Pham, M.S., Iadicola, M., Creuziger, A., Hu, L., Rollett, A.D., 2015. Thermally-activated constitutive model including dislocation interactions, aging and recovery for strain path dependence of solid solution strengthened alloys: Application to AA5754-O. Int. J. Plast. 75, 226-243.

Philippart, I., Rack, H.J., 1998. High temperature dynamic yielding in metastable Ti–6.8Mo–4.5F–1.5Al. Mater. Sci. Eng. A 243, 196-200

Poletti, C., Germain, L., Warchomicka, F., Dikovits, M., Mitsche, S., 2016. Unified description of the softening behavior of beta-metastable and alpha+ beta titanium alloys during hot deformation. Mater. Sci. Eng. A 651, 280-290.

Randau, C., Garbe, U., Brokmeier, H.G., 2011. StressTextureCalculator: a software tool to extract texture, strain and microstructure information from area-detector measurements. J. Appl. Cryst. 44, 641-646.

Rollett, A.D., Rohrer, G.S., Suter, R.M., 2015. Understanding materials microstructure and behavior at the mesoscale. MRS Bull. 40, 951-960.

Rollett, A., Rohrer, G.S., Humphreys, J., 2017. Recrystallization and related annealing phenomena, third ed. Elsevier.

Shi, R., Wang, Y., 2013. Variant selection during α precipitation in Ti–6Al–4V under the influence of local stress – A simulation study. Acta Mater. 61, 6006-6024.

Sidor, J.J., Decroos, K., Petrov, R.H., Kestens, L.A.I., 2015. Evolution of recrystallization textures in particle containing Al alloys after various rolling reductions: experimental study and modeling. Int. J. Plast. 66, 119-137.

Srinivasan, R., 1992. Yield points during the high temperature deformation of Ti-15V-3Al-3Cr-3Sn alloy. Scr. Metall. Mater. 27, 925-930.

Sun, Z.C., Wu, H.L., Cao, J., Yin, Z.K., 2018. Modeling of continuous dynamic recrystallization of Al-Zn-Cu-Mg alloy during hot deformation based on the internal-state-variable (ISV) method. Int. J. Plast. 106, 73-87.

Tasan, C.C., Hoefnagels, J.P., Diehl, M., Yan, D., Roters, F., Raabe, D., 2014. Strain localization and damage in dual phase steels investigated by coupled in-situ deformation experiments and crystal plasticity simulations. Int. J. Plast. 63, 198-210.

Wang, J., Moumni, Z., Zhang, W., 2017. A thermomechanically coupled finite-strain constitutive model for cyclic pseudoelasticity of polycrystalline shape memory alloys. Int. J. Plast. 97, 194-221.

Warchomicka, F., Stockinger, M., Degischer, H.P., 2006. Quantitative analysis of the microstructure of near β titanium alloy during compression tests. J. Mater. Process. Technol. 177, 473-477.

Weiss, I., Semiatin, S. L., 1998. Thermomechanical processing of beta titanium alloys—an overview. Mater. Sci. Eng. A 243, 46-65.

Xiao, Y., Zeng, P., Lei, L., 2018. Micromechanical modeling on thermomechanical coupling of cyclically deformed superelastic NiTi shape memory alloy. Int. J. Plast. 107, 164-188.

Zhang, Y.D., Wang, S.Y., Esling, C., Lecomte, J.S., Schuman, C., Zhao, X., Zuo, L., 2011. A method to identify dislocations in a known crystal structure by transmission electron microscopy. J. Appl. Crystallogr. 44, 1164-1168.

Zheng, Z., Waheed, S., Balint, D.S., Dunne, F.P.E., 2018. Slip transfer across phase boundaries in dual phase titanium alloys and the effect on strain rate sensitivity. Int. J. Plast. 104, 23-38.

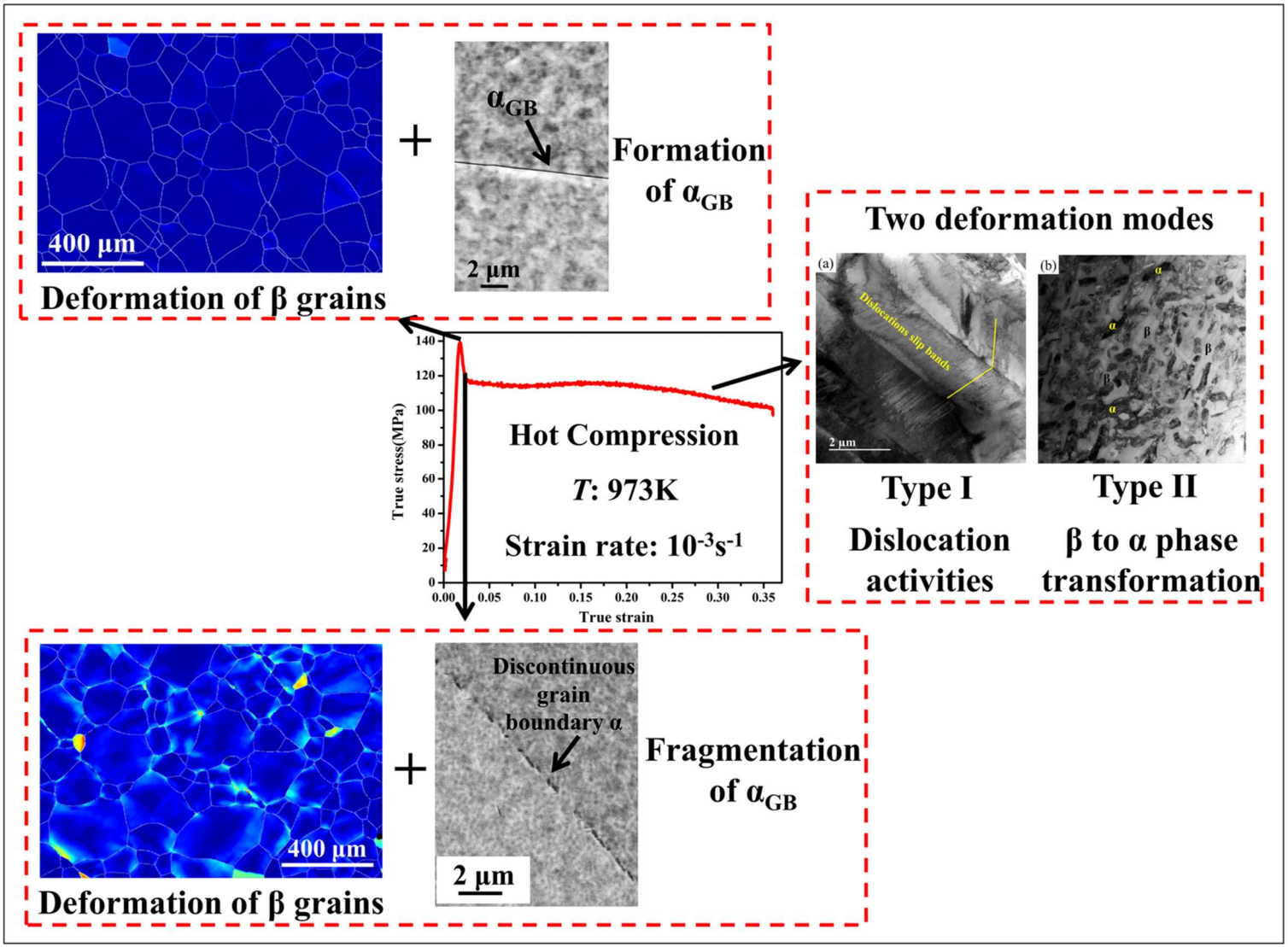
400 μm
Deformation of β grains
+
α_{GB}
2 μm
Formation of α_{GB}
Two deformation modes
(a)
Dislocations slip bands
2 μm
(b)
α
β
Type I
Dislocation activities
Type II
β to α phase transformation
True stress(MPa)
True strain
Hot Compression
T: 973K
Strain rate: $10^{-3}s^{-1}$
Discontinuous grain boundary α
2 μm
Fragmentation of α_{GB}
400 μm
Deformation of β grains